2014-05

Modeling pitting corrosion by means of a 3D discrete stochastic model

Corrosion Science,Amsterdam : Elsevier,v. 82, p. 133-144, May 2014
http://www.producao.usp.br/handle/BDPI/50302

Corrosion Science 82 (2014) 133–144

Contents lists available at ScienceDirect

Corrosion Science

journal homepage: www.elsevier.com/locate/corsci

Modeling pitting corrosion by means of a 3D discrete stochastic model

Pieter Van der Weeën [a,*], Alexsandro M. Zimer [b], Ernesto C. Pereira [b], Lucia H. Mascaro [b], Odemir M. Bruno [c], Bernard De Baets [a]

[a] KERMIT, Department of Mathematical Modelling, Statistics and Bioinformatics, Ghent University, Coupure links 653, B-9000 Ghent, Belgium
[b] Laboratório Interdisciplinar de Eletroquímica e Cerâmica (LIEC), Universidade Federal de São Carlos, Chemistry Department, 676, 13565-905 São Carlos, São Paulo, Brazil
[c] Instituto de Ciências Matemáticas e de Computação, Universidade de São Paulo, Av. do Trabalhador Sãocarlense, 400, 13560-970 São Carlos, São Paulo, Brazil

ARTICLE INFO

Article history:
Received 12 November 2013
Accepted 20 January 2014
Available online 28 January 2014

Keywords:
A. Steel
B. Modeling studies
C. Pitting corrosion

ABSTRACT

Pitting corrosion is difficult to detect, predict and design against. Modeling and simulation can help to increase the knowledge on this phenomenon as well as to make predictions on the initiation and progression of it. A cellular automaton based model describing pitting corrosion is developed based on the main mechanisms behind this phenomenon. Further, a sensitivity analysis is performed in order to get a better insight in the model, after which the information gained from this analysis is employed to estimate the model parameters by means of experimental time series for a metal electrode in contact with different chloride concentrations.

1. Introduction

One of the forms of corrosion that can be identified based on the morphology of the corroded metal is pitting corrosion [1]. This form of localized corrosion is restricted to small areas and can be recognized by the appearance of small holes on the metal surface as shown in Fig. 1 [2,3].

The first step in the pitting corrosion process is the passivity breakdown and the initiation of a localized attack, which can be brought about by various mechanisms [4,5]. Firstly, the environment of the metal can possess several critical conditions leading to the breakdown of the film in small areas, while preventing dissolution of the entire surface cover [6]. Secondly, the breakdown of the passive film can occur due to special features of the cover itself. Films are generally crystalline or get crystalline with time such that local thinning mechanisms, related to the nanostructure of the barrier layer that consists of nanograins separated by grain boundaries, render these regions susceptible to the pit nucleation process [4]. Besides crystalline grains in the passive film, other point defects are assumed to be electrons, holes, and oxide vacancies [7]. Finally, local depassivation can also be promoted by the presence of impurities or irregularities on the metal surface. All metals or alloys have some physical or chemical inhomogeneities that make them more susceptible to attack in aggressive environments compared to the remaining surface [8]. The chemical composition of the surface will affect the protective properties of passive films more severely than physical defects in the film [8]. These chemical inhomogeneities can be boundaries between the metal matrix and inclusions or between second phase precipitates [9]. Therefore, pits can nucleate at grain boundaries [8], on the grains itself [10], at mechanical damages [11], in heat-affected weld zones [12], dislocations [13] and at defects or inclusions (e.g. MnS, oxides, sulfides, silicates, precipitates of carbides and carbonitrites) in the microstructure of many metals or alloys [14]. When the pitting corrosion is promoted by the presence of inclusions in the metal surface [8,9], the shape of the pits can be modified by them as shown by Vignal et al. [14] and Gahari et al. [15]. In the latter, for example, the authors showed that the orientation of a MnS inclusion can be important for the pit evolution.

After the pit initiation in these regions, the acidity inside the pit is maintained by the spatial separation of the cathodic and anodic half-reactions, which creates a potential gradient and electromigration of aggressive anions into the pit [16]. As pit growth progresses, different solution compositions develop inside the cavity and the consequent voltage (IR) drop along the metal/electrolyte interface dictates that the deeper the pit is, the lower the pit growth rate is [17–19]. In addition, the formation of a lacy metal cover over a growing pit could occur. This cover provides a diffusion barrier which stabilizes the pit growth since it keeps the bottom of the pit in active dissolution [20].

Distributions and characteristics of pitting sites on metal surfaces have been determined through microscopic inspection [21,22]. The metal surface apparently has a fixed number of these inclusions, i.e. sites for pit nucleation, as observed in recent works by Punckt et al. [21] and Zimer et al. [22]. The absence of pit creation at close distance of already existing pits is another issue

* Corresponding author. Tel.: +32 92645931; fax: +32 92646220.
E-mail address: pieter.vanderweeen@ugent.be (P. Van der Weeën).

http://dx.doi.org/10.1016/j.corsci.2014.01.010
0010-938X/

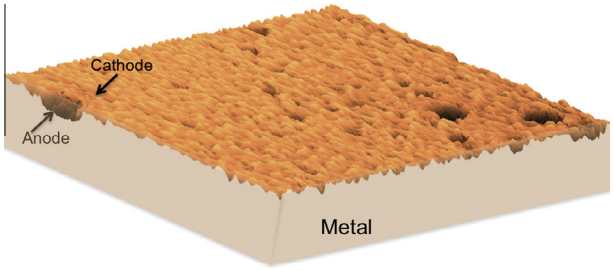

Fig. 1. Pitting corrosion with indication of anodic and cathodic half-reactions.

that is studied. Reuter and Heusler [13] showed that the probability of finding no pit decreases exponentially with the area around an active pit. This produces an exclusion zone of a few μm around each active pit in which new pits cannot be nucleated [13]. González-García et al. [23] detected anodic and cathodic current transients on 304 grade austenitic stainless steel by scanning electrochemical microscopy (SECM) measurements. The microscope tip, set to detect the Fe^{2+} in the anolyte from the metastable pits, detects the reduced background of cathodic current after the anodic transient associated with the pit itself.

A better understanding of the pitting corrosion phenomenon is necessary to combat its destructive effects [1,24]. Even a small pit with minimal overall metal loss can lead to the failure of an entire engineering system because of others corrosion types that can stem from pitting corrosion such as stress corrosion cracks [8,25,26]. Therefore, pitting corrosion has been widely studied for many years. Nevertheless, some aspects of these phenomena remain unclear. Modeling and simulation enables us to understand and predict the nature and intensity of corrosion, eliminates the need for difficult experimental measurements of corrosion under different electrochemical conditions and allows for extrapolating over longer time scales and to other physical conditions. However, the modeling of the corrosion phenomenon is challenging due to its complex nature and the involvement of many variables and consequently up till present, no satisfactory, validated models exist [17].

In the second half of the 20th century, initial corrosion models, mostly based on (partial) differential equations ((P)DEs), were used to describe either the initialization of corrosion [27,28] or the propagation of corrosion [29–31]. Later on, models were introduced incorporating both steps, more processes such as passive film formation were added and specific models for specific conditions were developed. Although these models are elaborate, they require extensive knowledge about the material, its origin and the process, which poses problems for both their development and more so for their validation [32]. Therefore, the use of new modeling paradigms such as artificial neural networks [33], statistical models [34] and cellular automata (CAs) are being explored [35].

In this paper, a three-dimensional CA-based model describing pitting corrosion is developed. The use of CAs in the field of corrosion is relatively new [36,37], but the number of researchers employing CAs as well as the knowledge on the subject is growing. Although many different aspects that influence corrosion, such as film formation, pH, potential differences and heterogeneous composition of alloys, are being explored and are incorporated in CA-based models, most of them only establish a qualitative resemblance between the simulated model output and the real-world phenomenon, ignoring the importance of a sound model validation that is a prerequisite to have a model with predictive value [2,17,19,38–41]. Only very recently, a few authors validated their CA-based model using time series of data, but with modest success [42]. Furthermore, CA-based models in literature are usually two-dimensional, making them unsuited to model the growth of corrosion pits in the direction of the pit depth and surface simultaneously [19]. Three-dimensional models could provide new information about dynamic processes like pit coalescence or the formation of channels and peninsulas inside the metal. Nevertheless, the simultaneous study of all factors involved in pitting corrosion is a complex task to overcome using a single approach. For that reason, the model introduced in this paper focuses on mass transport, IR drop, pit initiation, metal dissolution and cathodic protection, but leaves aspects such as passivation and bimetallic corrosion with spatially different behavior towards corrosion, aside for the time being.

In Section 2 of this paper, some background is provided on the CA paradigm, the experimental set-up through which the data used in this paper were obtained as well as the construction of the stochastic 3D CA-based model. The sensitivity analysis and the parametrization of the developed model form the subject of Section 3, while the conclusions and the future work are discussed in Section 4.

2. Material and methods

2.1. Cellular automata

CAs are mathematical constructs in which the space, state and time domains are discrete as opposed to PDEs in which these three domains are continuous [43,44]. The ability of CAs to generate a rich spectrum of sometimes complex spatio-temporal patterns from relatively simple underlying transition functions has led to their successful employment in the study of several (a)biological processes [45–50]. Models based on CAs can be seen as an alternative to PDE-based models, to provide researchers with a wider range of modeling tools and, in some complex cases, a solution to problems encountered with some of the more classical modeling methods [51,52].

2.1.1. Choice of an appropriate model

Important when developing a model is the choice of method and particularly the level of description, be it microscopic, mesoscopic or macroscopic. Microscopic description of the Monte Carlo or molecular dynamics type are not interesting for pitting corrosion since this is a rather scarce event on the atomic scale. With the size of the corrosion pits in the range of 10–100 nm, the time and space scales of the phenomenon are far beyond the reach of the present-day atomistic level computations [38]. On the other hand, a macroscopic description with classical kinetic equations, normally based on a system of PDEs, poses the problem that in most cases analytical solutions of the resulting equations are not at hand. For that reason, some kind of discretization has to be used to be able to solve the problem numerically, which unavoidably gives rise to approximation errors and stability problems [51,52]. Finally, the macroscopic modeling of electrochemical reactions is unable to capture the stochasticity of the corrosion processes causing that some of the information, important to engineers, is not readily available [42]. The mesoscopic approach is seen as a way to combine the macroscopic phenomenology with the stochastic character of the processes originating from the microscopic scale processes [53]. CAs lend themselves to construct mesoscopic models that describe the evolution of metal surface related to stochastic processes while adhering to a realistic electrochemical point of view. However, it is not the goal to describe a specific system but rather to analyze how a combination of a small number of basic processes, very well accepted by electrochemists, might determine general features.

Another advantage of employing CA-based models is that they are so-called gray-box models that stand between white-box models, which are based on a detailed understanding of the underlying physical laws and processes, and black-box models, which simply reproduce the input–output behavior of the system but make no use of physics or chemistry [42]. Like the black-box models, the gray-box models are parametric models where the parameters are learned from data, but the difference with black-box models is that here the parametric model is motivated by basic physical ideas instead of simply being selected from a class of universal approximators. Usually gray-box models are characterized by smaller parameter sets and the parameters themselves yield some physical insight into the problem. This approach allows for constructing a mathematical model that describes the complex pitting corrosion phenomenon using the knowledge that is available without the necessity to know the governing processes and equations exactly.

2.1.2. Paradigm

In this paper, we make use of a homogeneous CA, in which a single transition function governs the dynamics of all cells. The following definition of a homogeneous 3D CA is relied upon.

Definition 1. (Homogeneous 3D cellular automaton)

A homogeneous 3D cellular automaton $\mathcal{C}$ can be represented as

$$\mathcal{C} = \langle \mathcal{G}, S, s, N, \Phi \rangle,$$

where

(i) $\mathcal{G}$ is a three-dimensional grid of cells c.
(ii) S is a finite set of h states, with $S \subset \mathbb{N}$.
(iii) The output function s yields the state $s(c,t)$ of every cell c at the tth discrete time step.
(iv) The neighborhood function N determines the neighboring cells of every cell c, including the cell c itself.
(v) The transition function Φ yields the state $s(c,t+1)$ of every cell c at the next time step, based on its state and that of its neighboring cells at the current time step.

For reasons of comprehensiveness, some parts of this definition will be elaborated here.

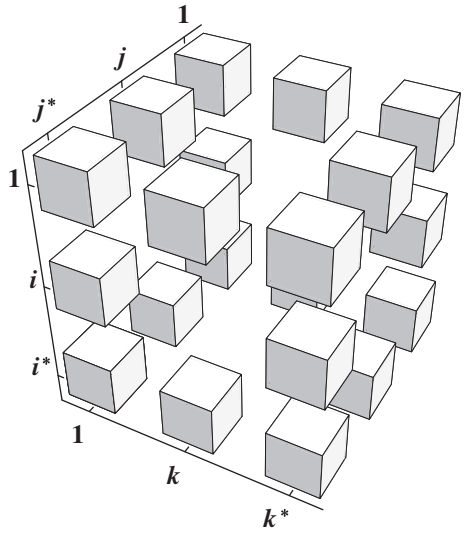

Fig. 2. Ordering of the cells of a 3D CA.

Grid $\mathcal{G}$. In this paper, a finite three-dimensional grid consisting of cubes is used, because it has the most straightforward implementation and suffices for the purposes of this paper. An indexing of the cells of a 3D CA is introduced, which is shown in Fig. 2, with i^*, j^* and k^* the number of layers, rows and columns, respectively. Therefore, i represents the thickness direction of the metal, while j and k together form the surface. This grid allows for modeling both the affected metal surface as well as the depth of the corrosion pits, both in function of time.

Neighborhood function N. Different neighborhoods can be defined in 3D, the two most important ones being the Moore and the von Neumann neighborhood. The Moore neighborhood of a cell $c_{i,j,k}$ comprises those cells that share at least a vertex with $c_{i,j,k}$ and thus counts 27 neighbors in total (see Fig. 3(a)). The von Neumann neighborhood is a more restricted neighborhood in which only those cells that share a face with $c_{i,j,k}$ are considered as neighbors giving rise to a total of 7 neighbors (see Fig. 3(b)).

Discrete states. Every cell $c_{i,j,k}$ has one of the h discrete states comprised in the set S. As this paper deals with a mesoscopic description of the corrosion phenomenon, cells are not to be associated directly with the individual atoms, anions or cations, but rather to a homogeneous grouping of the same type of atom. The latter means that atomic size effects are not accounted for [54], which is a simple approximation intended to capture the synoptic effects of pitting corrosion [55,56]. The states of the cells $c_{i,j,k}$ of $\mathcal{G}$ at $t = 0$, i.e. $s(c_{i,j,k}, 0)$, constitute the initial condition of $\mathcal{G}$.

Transition function Φ. The transition function Φ determines the state of a cell $c_{i,j,k}$ at the $(t+1)$th time step based on the cell's current state and the states of its neighboring cells and is devised as to mimic, as closely as possible, the physicochemical processes involved in pitting corrosion at a mesoscopic level [38]. The transition function Φ that is used in the remainder of this paper is executed in a stochastic and synchronous manner. The former means that the application of the transition function Φ is subject to a probability P and will therefore not necessarily be evaluated at every consecutive time step. This entails that the outcome of a stochastic CA-based model differs for every simulation. Evaluating Φ in a synchronous manner means that all cells update their state at the same time ([57]).

2.2. Experimental procedure

2.2.1. Experimental conditions

Pitting corrosion on AISI 1040 steel was performed in a hydrogen carbonate solution (0.1 mol dm^{-3}) prepared by the dissociation of $NaHCO_3$ (Merck) in deionized water at pH 8.3. Prior to

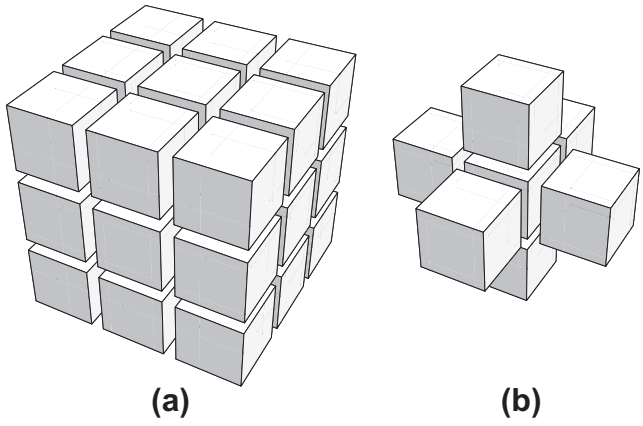

Fig. 3. Neighborhoods of a cell $c_{i,j,k}$ in a 3D grid: (a) Moore neighborhood and (b) von Neumann neighborhood.

data acquisition, the solution was deaerated for 10 min with N_2. The study of the influence of the chloride concentration during pit initiation and propagation was performed using following weight percentages: 2.25, 2.5 and 3.5 wt.% of NaCl (JT Backer) in the solution. Further, cylindrical steel samples (Sanchelli) with a diameter of 9.5 mm ($A = 0.7$ cm^2) were used as the working electrode (WE). The WEs were previously abraded with sandpaper up to 2000-grit, polished with diamond paste (1 and 0.25 μm), and degreased in acetone for 1 min in an ultrasonic bath. The material composition is described in a previous paper [22]. As the reference electrode (RE) and auxiliary electrode (AE), Ag/AgCl/KCl (saturated) and a Pt wire were used, respectively.

2.2.2. Data acquisition

Two types of electrochemical measurements were performed with an Autolab model PGSTAT 30, being the open-circuit potential (E_{oc}) and chronoamperometric measurements. A homemade flat-bottom cell, previously described in literature [58], was employed in these experiments. The use of this cell enables the coupling of the electrochemical techniques and measurements with *in situ* temporal series of micrographs (TSM) obtained with an inverted optical microscope (OM), brand Opton model TNM-07T-PL. The software tools Scope Photo® 1.0 and MCDE (AMCAP) were used for the data acquisition.

In this approach, the E_{oc} was followed up to its stabilization during 6000 s. After stabilization, all chronoamperometric measurements were performed for 1800 s with an overpotential (η) of 350 mV more positive than E_{oc}. At the same time, an area of 680 μm × 544 μm, i.e. 0.52% of the WE, was recorded using an acquisition rate of 0.05 and 1 image per second during the E_{oc} and chronoamperometric measurements, respectively. The optimization of the overpotential η to be applied during the chronoamperometric measurements was investigated at a low chloride concentration of 1.5 wt.%. The value of 350 mV was chosen because it allows for observation of the first pit nucleation when verifying the *in situ* image of the electrode surface. It is noted here that different areas of 680 μm × 544 μm of the WE electrode were followed in order to assure that this small part of the surface was representative of the whole process occurring during the measurements. Starting at the center of the WE, where the TSM were collected, the electrode surface was studied towards the corners of the sample in the orthogonal directions. Thus, several *in situ* micrographs were collected for these new positions and they were compared with the last frame of the temporal series. For each experimental condition, the pit dispersion in the final frame of the studied time series was similar to the dispersion of the rest of the electrode surface, excluding edge effects.

To convert the images (frames) from the TSM into quantitative information, a procedure previously described in literature [22,59] was employed. The number of pits and total pit area were obtained from the *in situ* TSM. The average pit depth was estimated using a fraction of the total charge consumed during the pit formation. This fraction of total charge changes in every frame according to the pit mouth area observed during chronoamperometric measurements. Finally, a three-dimensional model of pit evolution based on Faraday's law was used to calculate the average pit depth and its evolution over time. Fig. 4(a)–(c) show the number of pits, the corroded surface area and the average pit depth, respectively, in function of time and for the different mass percentages of chloride ions in solution. It is noticed from Fig. 4(a) that a maximum number of pits is reached for 2.5% chloride in solution instead of for 3.5%. Although not completely elucidated, the explanation seems to lie in a shift in corrosion emphasis dependent on the chloride concentration. At lower concentrations of chloride, more pits are formed than at higher concentrations, but these pits are volume-wise smaller. One possible explanation is that the higher diffusion gradient at higher chloride concentrations forces the chloride cells more towards the inside of the pits. This explains that although 3.5% chloride in solution does not yield the highest number of pits, the total affected surface and the average pit depth at 3.5% chloride is the highest. More details on the procedure and data can be found in Zimer et al. [60].

2.3. Model development

In this paper, a stochastic 3D CA-based model describing pitting corrosion is proposed. A grid $\mathcal{G}$ consisting of 151 × 200 × 200 cubes is used where the top layer, i.e. $s(c_{1,j,k}, t)$, represents the aqueous solution containing the corrosive agent while the other 150 layers represent the metal subjected to corrosion. The number of cells is chosen as such to obtain a small enough grid resolution to prevent overly sensitive model parameters that result in very fluctuating solutions from simulation to simulation, while still not resulting in excessive computation times. Along the j- and k-axes periodic boundary conditions apply, meaning that the cells of the first row (column) are considered to be adjacent to those of the last row (column) to avoid border effects [2]. Along the i-axis on the other hand, fixed boundary conditions are employed since the top layer (aqueous solution) and bottom layer (metal) of $\mathcal{G}$ do not physically form an interface and so through these boundaries no movement is possible. A schematic representation of the grid $\mathcal{G}$ is shown in Fig. 5. The metal part of the grid $\mathcal{G}$, i.e. the bottom 150 layers, represents only a part of the studied electrode surface used for the data collection to get a resolution fine enough to approximate the experimental results as well as to avoid excessive computation times. By presuming Δj and Δk to be 1.24×10^{-6} m and $\Delta i = 1.44 \times 10^{-7}$ m, the grid captures one sixth of the total studied electrode surface area and has a maximum depth large enough to allow for the maximum average experimental pit depth (see Fig. 4(c)) to occur. The solution in which the metal electrode is submerged is represented here initially by a single layer wherein chloride can diffuse. Since the modeling interest lies in capturing the pitting initiation and propagation processes, in this way the computationally demanding diffusion process is kept to a minimum.

Further, three different discrete states, i.e. S = {water, chloride, metal}, are discerned. Although the corrosive solution contains more components than merely water and chloride, here all the non-reactive components are considered as water since they are irrelevant for the current modeling purposes. The initial condition of $\mathcal{G}$ is determined by the experimental set-up (see Section 2) meaning that initially no pits are present in the metal such that all cells of layer two up to layer 151 of $\mathcal{G}$ have state metal at $t = 0$. In layer 1, a number of cells is assigned the chloride state according to the mass percentage of chloride in the solution and is randomly distributed across this layer, while the rest of the cells gets assigned the water state.

The transition function Φ falls apart into three parts that describe diffusion, pit initiation and pit propagation, respectively. For the first part of the transition function, only the cells in the chloride state are evaluated, since only their movement is both possible and relevant. Every cell in the chloride state can move once via diffusion in each time step. The motion dynamics of a cell in state chloride are simulated by switching the state of the central cell $c_{i,j,k}$ and the state of the cell in its neighborhood it moves towards. To comply with the law of mass conservation, if more than one cell in state chloride tries to move to the same cell, none of them is allowed to move. The complete reaction and diffusion neighborhood N^* employed in this paper is the 3D Moore neighborhood depicted in Fig. 3(a). However, depending on the position of $c_{i,j,k}$, N^* can be truncated to fit the fixed boundaries of the system. Initially, a random neighbor of $c_{i,j,k}$ in N^* is chosen to move towards after which it is checked whether this cell is in the water

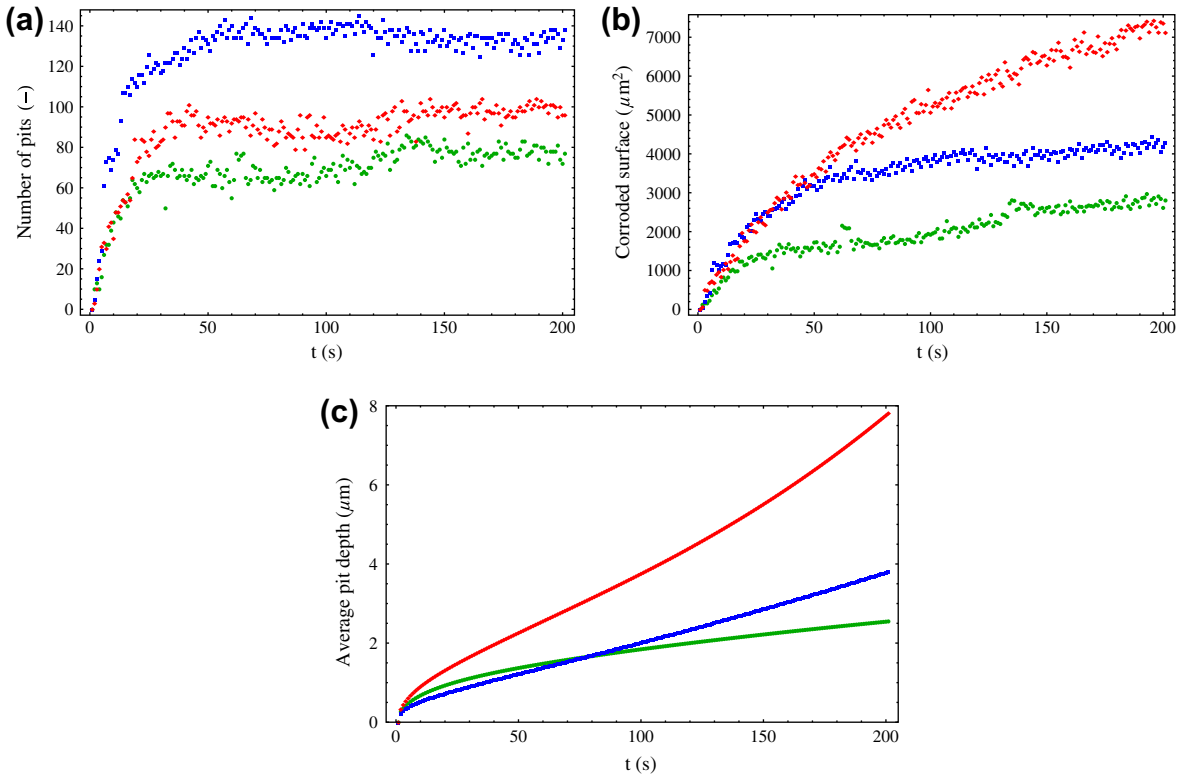

Fig. 4. Experimental data: (a) number of pits, (b) corroded surface area and (c) average pit depth in function of time for mass percentages of 2.25% (green, circles), 2.5% (blue, squares) and 3.5% (red, diamonds) of chloride ions in corrosive solution. (For interpretation of the references to colour in this figure legend, the reader is referred to the web version of this article.)

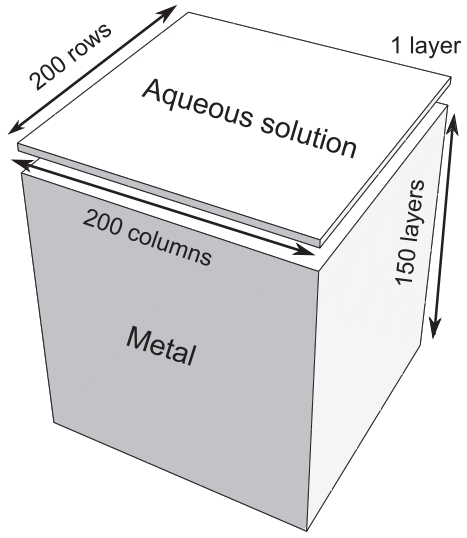

Fig. 5. Schematic representation of the 3D grid.

state and is therefore a viable candidate to move towards. Nevertheless, once pits appear on the surface and grow, a concentration and potential gradient emerges and chloride will preferably move (deeper) inside the pits. To capture this, a suction probability $\iota \in [0, 1]$ is introduced that indicates whether or not chloride moves towards the lowest possible position in N^* with certainty or if any free position in N^* is chosen at random. Furthermore, since the diffusion coefficient of chloride in these specific conditions is not known, Δt, i.e. the number of seconds corresponding to one discrete time step of the CA-based model, is set as a model parameter. The total number of time steps the CA-based model is denoted t_n and is given by Eq. (1):

$$t_n = \lfloor 200/\Delta t \rfloor. \tag{1}$$

It is pointed out here that a calibrated value for Δt will not depend on the experimental data alone, but also on the values chosen for $\Delta i, \Delta j$ and Δk, since the cell dimensions and the time step can not be chosen independently and are connected via the diffusion coefficient [39].

The second part of Φ is the pit initiation where surface metal cells, i.e. where $s(c_{2,j,k}, t) =$ metal, get their state changed to state water or chloride, based on the same ratio as the grid initiation, with a probability P_p through an attack of a cell in the chloride state. An attack of a cell in the chloride state starts, like the diffusion part of Φ, by choosing another cell in its neighborhood N^* to direct its attack towards. Firstly, it is checked whether the selected cell is a surface metal cell. The next step is verifying whether the cell under attack is not already protected through cathodic protection. This latter phenomenon occurs when the metal surface around a newly formed or growing pit becomes negatively charged (see Section 1) as such preventing the appearance of new pits in close vicinity of existing pits. The radius of the exclusion zone for each active pit here is taken as 5 μm, based on previous works and observations of the *in situ* images from the metal surface. Translating this cathodic protection to the grid $\mathcal{G}$, a protection distance of four cells is taken around any existing pit. Finally, an attack only becomes effective with a probability $P_p \in [0, 1]$. From the experimental data (cf. Fig. 4(a)) a maximal number of pits for each chloride concentration is deduced and when this maximum is reached, P_p is set to 0 from that point on, as such preventing the formation of new pits.

The pit propagation or pit growth, both on the surface as in the depth, forms the final part of the transition function Φ. As for the

pit initiation, metal cells get their state changed to water or chloride, based on the same ratio as the initiation of $\mathcal{G}$, after an attack by a cell in the chloride state. However, unlike for the pit initiation, the candidate metal cells for attack are metal cells that are part of an already existing pit. In this part of Φ, all chloride cells choose one of their Moore neighbors at random to attack, and when this neighbor is a metal cell belonging to a pit edge, this metal is dissolved with a probability P_d. There is an indubitable IR control of the current pit growth laws [17,18] and therefore the IR-factor is incorporated in the CA-based model as a parameter $\zeta \in [0, 1]$. This parameter is used together with the dissolution probability without potential gradient (i.e. the dissolution probability at the metal surface) P_{d0}, again $\in [0, 1]$, to calculate P_d in the following manner [17]:

$$P_d = P_{d0}\left(1 - \frac{\zeta d}{d_m}\right), \tag{2}$$

with d the depth of the metal cell under attack and d_m the total depth of the metal layer, i.e. 150 cells. From Eq. (2), it can be seen that with the IR drop the dissolution probability decreases with increasing pit depth.

Table 1 gives an overview of the model parameters that need to be calibrated using the experimental data from Section 2 and Fig. 6 shows a flow chart of the CA-based model.

3. Results and discussion

All code is written in Mathematica 9.0 and simulations are performed on a Dell Optiplex 780 with an Intel Core 2 Quad Q9400/2.66 GHz, 6 M, 1333FSB processor. Simulation time is dependent on the parameter setting and ranges for the relevant parameter settings in this paper from 20 min to 45 min. The Mathematica source code is available upon request.

3.1. Sensitivity analysis

Sensitivity analysis (SA) has long proven its use in model building, since often model parameters are uncertain, especially when modeling complex natural systems [61,62]. It provides model builders with useful insights into the level of uncertainty contributed by each parameter, which can be important for research prioritization, decision making during parametrization and reducing the model complexity by filtering out parameters that have a minor effect on the model outcome.

In deterministic models, the outcome for a specific set of parameters is essentially the same for identical initial conditions. Stochastic models, like the one used in this paper, on the other hand, have varying outputs between simulations, even if parameter values and initial conditions are identical [63]. Rather than comparing two single output values for sensitivity analysis, as is the case for deterministic models, two distributions of output values have to be compared. SA for stochastic models is often based on the mean of the different distributions of output values, although a better approach also accounts for the shape of the distributions, for instance by taking into account the variance [62].

Table 1
Overview of model parameters.

Symbol	Description	Range	Unit
ι	Suction probability	[0,1]	–
Δt	Physical time for one discrete time step	[0,200]	s
P_p	Pit initiation probability	[0,1]	–
P_{d0}	Dissolution probability at metal surface	[0,1]	–
ζ	IR drop	[0,1]	–

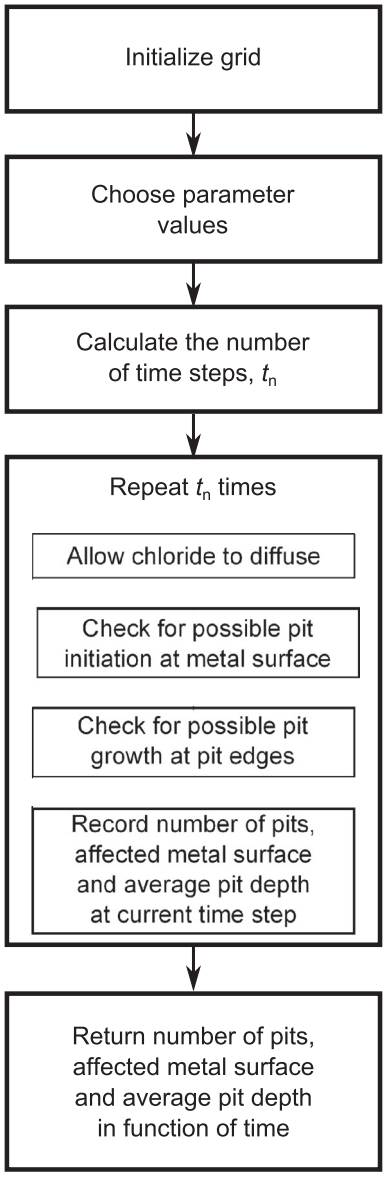

Fig. 6. Flow chart of CA-based model.

Furthermore, since simulations with CA-based models are generally more time consuming, a screening method for SA is adopted here because such method has a relatively low computational cost when compared to other approaches. With screening methods, the objective is to identify which input variables are contributing significantly to the output uncertainty, rather than exactly quantifying sensitivity.

An effective screening method for SA is the variance-based Elementary Effects (EE) method, where basic statistics are computed to obtain sensitivity information [64–66]. Here, the calculation of the sensitivity H_l of the model output Y to a single parameter q_l is repeated r times and the mean μ_l and standard deviation σ_l of these r computations are used to assess the importance of parameter q_l. Often it is useful to compute μ_l^*, being the mean of $|H_l|$ as it comes at no extra cost to calculate and resolves the issues encountered with non-monotonic models. The importance of the different parameters can be assessed graphically using a (μ^*, σ) plot, with the parameters closest to the origin being the least influential [67]. Although widely and successfully used in literature and recently also for stochastic biological models [68], the

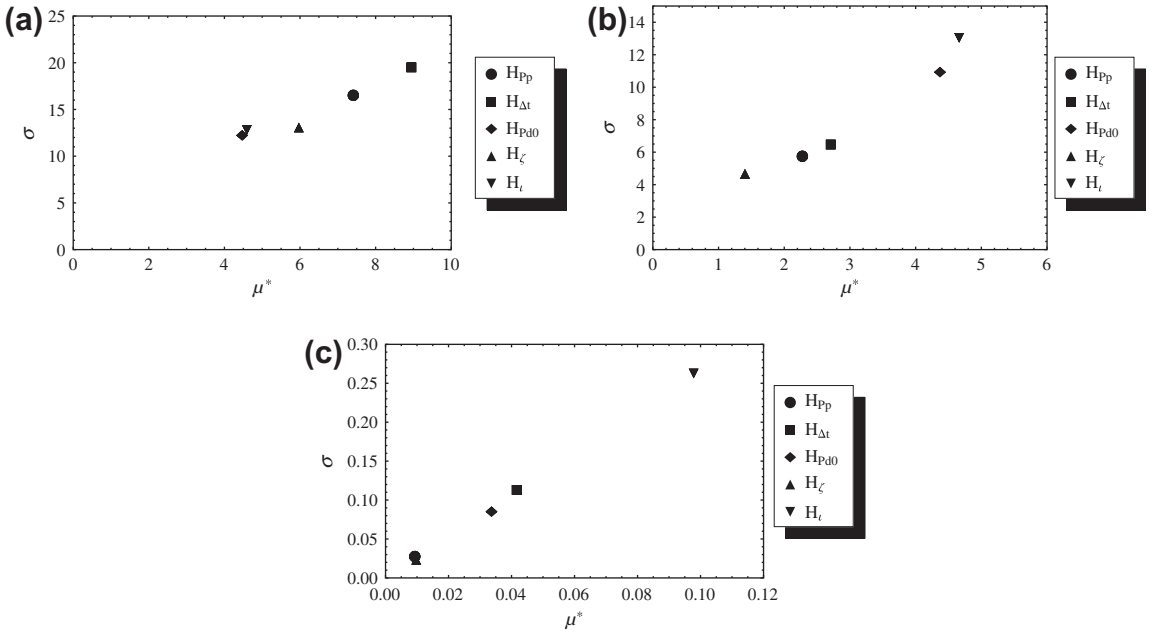

Fig. 7. Screening of the parameters based on the EE method for three data sets: (a) number of pits, (b) corroded surface and (c) average pit depth in function of time for a mass percentage of chloride ions in corrosive solution of 3.5%.

use of this SA technique for CA-based models is to the authors' knowledge very limited.

The SA results that follow next are obtained for a mass percentage of chloride ions of 3.5%, but uphold for the two other concentrations. From Fig. 7(a) it can be concluded that with regard to the number of pits in function of the time, parameters Δt and P_p are the most sensitive, since the sensitivity measures for these parameters are the furthest removed from the origin. This result was expected, because these two parameters together state the probability of a new pit appearing at a certain moment in time. Analogously, from Fig. 7(b) it can be seen that parameters P_{d0} and $\imath$ are the ones that most influence the affected metal surface in function of time. This again is a logical outcome since P_{d0} is the probability that a metal cell pertaining to an already formed pit dissolves while $\imath$ dictates the preference of a corrosive agent to stay in the neighborhood where it is by random movements or move preferentially towards the bottom of the existing pit. Finally, Fig. 7(c) shows that the average pit depth in function of time is clearly most sensitive to the value of $\imath$, which could also be anticipated.

3.2. Inverse problem solving

3.2.1. Optimization method

The remainder of this section deals with solving the inverse problem, i.e. retrieving the values of the model parameters from Table 1, belonging to the observed data from Fig. 4(a)–(c) for each of the three different chloride concentrations. This comes down to estimating five parameters, making use of three time series of data (number of pits, affected surface area and average pit depth). Two measures of fitness between the observed data and the corresponding simulated time series with the CA-based model are used. The absolute error (AE) is used between the experimental and simulated number of pits in function of time, since this is a discrete measure, and the root mean squared error (RMSE) is used for the remaining two time series.

The optimization method used in this paper to minimize the AE and the RMSE is a grid search [69]. Similar research questions in literature have been tackled by iterative optimization using the Nelder and Mead method and genetic algorithms [42]. However, when parametrizing models that give rise to multiple local optima and where one model evaluation is highly time consuming, which is often the case for CA-based models, unnecessary model evaluations should be avoided and more protection against local optima is desired [47,70]. Furthermore, when several computer nodes are at disposal for calculating several solutions simultaneously, iterative heuristics pose a problem, since a calculation is always based on the previous result. In these cases a grid search, which evaluates the model in a number of predefined points in the parameter space, is the preferred procedure, especially when the number of parameters to be determined is not excessive.

3.2.2. Parametrization of the CA-based model

Initial attempts of the authors to estimate all five parameters simultaneously using a grid search have proven unfruitful, probably due to the complex nature of the CA-based model. Therefore, the information gained from the SA is employed during the parameter estimation process to overcome this problem. In a first step, only $\imath, \Delta t$ and P_p are estimated using the time series of the number of pits, while P_{d0} and ζ are given a constant value of 0.3. This is justified, since the former three parameters are the most sensitive model parameters for this output and therefore determine predominantly whether the number of pits in function of time can be correctly predicted. Then, in a second step, using the optimal values for $\imath, \Delta t$ and P_p found in the first step, P_{d0} and ζ are estimated using the two time series that have not yet been used, being the affected surface area and the average pit depth. In what follows,

Table 2
Selected subspace of the search space for the model parameters.

Symbol	Subrange
$\imath$	[0, 1]
Δt	[0.2, 1.2]
P_p	[0, 0.001]
P_{d0}	[0, 1]
ζ	[0, 1]

this approach is elaborated on for a mass percentage of chloride ions of 3.5%.

Some preliminary model exploration allowed to select a subspace of the search space defined in Table 1, which is represented in Table 2. The subrange of Δt is explained by the fact that values that are too small increase computation times beyond the desirable time a modeler wants to wait for results, while values that are too large are not able to capture the observed data to an acceptable precision. A small value for P_p is also expected since a limited number of pits has to be initiated with a relatively large number of cells in the chloride state being able to attack the metal surface.

By means of a Sobol sequence [71], 2000 combinations of $\imath, \Delta t$ and P_p are chosen from their subranges as presented in Table 2 in order to get a good coverage of this subspace and as mentioned before $P_{d0} = \zeta = 0.3$. An evaluation with the CA-based model is performed with each of the 2000 parameter combinations, the simulated number of pits in function of time is determined, after which the AE is calculated with the experimental data at every point of the time series. Since the proposed CA-based model is stochastic in nature, model evaluations with the 200 parameter combinations that give rise to the lowest AE, are performed in tenfold to account for the stochasticity. Subsequently, from the ten repetitions, the average result is calculated and again the AE is calculated, after which the parameter combination that results in the lowest average AE is selected as the optimal combination. It is worth mentioning that different combinations can result in similar solutions due to equifinality [72]. This is explained by the fact that increasing both Δt and P_p to a certain Δt^* and P_p^* can result in more or less the same simulated output. However, in order to compare the optimal parameter values for different chloride concentrations, a same Δt has to be chosen for all three concentrations. Therefore, a relatively small Δt is selected in order to approximate the observed data for the different concentrations. The obtained optimal parameter values are: $\imath = 0.503, \Delta t = 0.399$ and $P_p = 0.000201$. Fig. 8 shows both the ten separate simulated outputs, the average simulated output and the observed number of pits in function of time.

Next, the optimized parameter values for $\imath, \Delta t$ and P_p are set as a constant for these parameters and 2000 combinations for P_{d0} and ζ are chosen using a Sobol sequence. The weighted RMSE is determined for each of the 2000 combinations. This is done by adding up the RMSE that is the result of the comparison between the simulated affected surface area and the experimental data represented in Fig. 4(b) and the RMSE that is the result of the comparison between the average pit depth in function of time and the experimental data represented in Fig. 4(c). Afterwards, simulations are again performed in tenfold with the 200 parameter combinations that result in the lowest weighted RMSE. It is mentioned here that for reasons of simplicity of the calculations, the data from Fig. 4(b) are expressed in the percentage of the metal surface that is affected instead of the surface area in μm^2. The optimal parameter values found here are $P_{d0} = 0.650$ and $\zeta = 0.918$ and the simulated outputs using these optimized values are shown in Fig. 9(a) and (b). It is clear from these figures and Fig. 8 that although the simulated output corresponds quite good with the observations, further improvement is possible. However, further simulations have shown that when optimizing the parameters for one time series of data, e.g. the number of pits, that a 'good' fit for the other two time series of data is not possible with the model in its current form. Therefore, a parameter combination is chosen that results in a simulated output that gives the best result when all three time series are considered simultaneously.

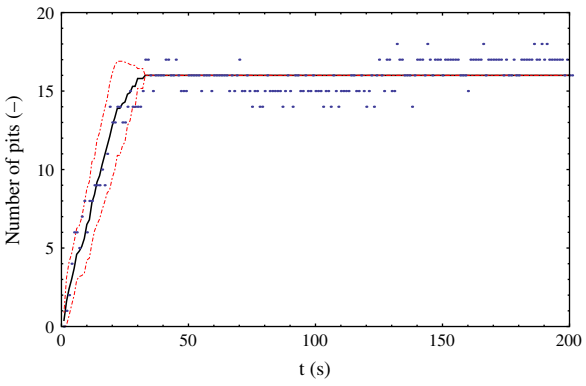

Fig. 8. Average simulated model output (black line) with $\imath = 0.503, \Delta t = 0.399, P_p = 0.000201, P_{d0} = 0.3$ and $\zeta = 0.3$, the confidence interval around this average output, constructed by the mean value at each point plus and minus the standard deviation of the ten repetitions (red dotdashed lines), and the observed number of pits (blue dots) in function of time for mass percentage of chloride concentration of 3.5%. (For interpretation of the references to colour in this figure legend, the reader is referred to the web version of this article.)

Fig. 10 (a)–(c) show one of the pits after 200 s as modeled with the CA-based model, i.e. the end of the experiment. These figures show that the pit grows in a circular shape at the surface, however, this is not the case for all pits that are created during simulations. This is realistic since pits preferentially grow along impurities on the surface, such as small scratches, and are therefore not necessarily circular in shape.

3.2.3. Influence of chloride concentration on optimized parameter values

The same procedure is used to estimate the parameters belonging to the three time series for the two remaining chloride concentrations, giving rise to the results in Table 3. It is clear that the optimized parameter values are dependent on the mass percentage of chloride ions. The suction strength $\imath$ is larger for the two highest concentrations since larger concentrations of chloride induce larger concentration and potential gradients, making the influence of this parameter on the diffusion direction of chloride increasingly more important. Moreover, the larger potential difference results in a rising value for ζ as can be read from the table. The obtained value for P_p increases from a mass percentage of chloride ions of 2.25% to 2.5% and decreases again from 2.5% to 3.5%. The total number of pits in function of time almost doubles going from a mass percentage of chloride ions of 2.25% to 2.5%, which can not be completely attributed to the (small) rise in the mass percentage and therefore a higher value for P_p is necessary. On the other hand, at a mass percentage of 3.5%, both the total number of pits in function of time is lower and the concentration is much higher, resulting in a lower value for P_p again. A similar trend as for P_p can be observed for P_{d0}. The increase in value for P_{d0} from a mass percentage of 2.25% to 2.5% can be explained by the larger affected surface and the higher average depth of the pits as seen in Fig. 4(b) and (c). Nevertheless, when the chloride concentration rises from 2.5% to 3.5%, the optimal value for P_{d0} drops. The cause for this drop in value is probably due to the combination of the higher chloride concentration on the one hand and the high value for $\imath$ on the other hand, keeping the chloride trapped inside the pit and produce the aforementioned results with regard to the affected metal surface and average pit depth.

3.3. Pitting corrosion in bimetals

There are many difficulties associated with the experimental measurements necessary to understand bimetallic corrosion, which is caused by the juxtaposition of two or more metals, and as a result a number of theoretical models of the various stages of this and other types of localized corrosion have been developed [6]. Therefore, in order to illustrate the potential of the developed

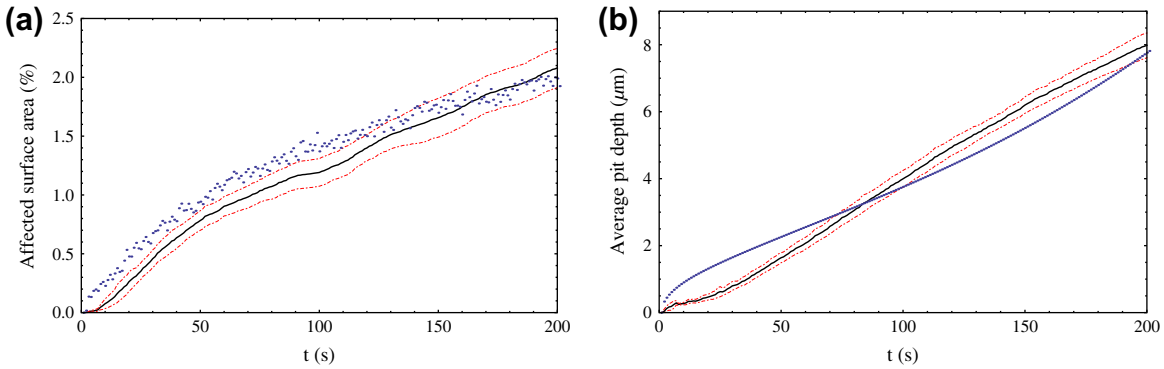

Fig. 9. Average simulated model output (black line) with $\iota = 0.503, \Delta t = 0.399, P_p = 0.000201, P_{d0} = 0.650$ and $\zeta = 0.918$, the confidence interval around this average output, constructed by the mean value at each point plus and minus the standard deviation of the ten repetitions (red dotdashed lines), and the observed data (blue dots) in function of time for a mass percentage of chloride ions of 3.5% for (a) the percentual affected metal surface and (b) average pit depth. (For interpretation of the references to colour in this figure legend, the reader is referred to the web version of this article.)

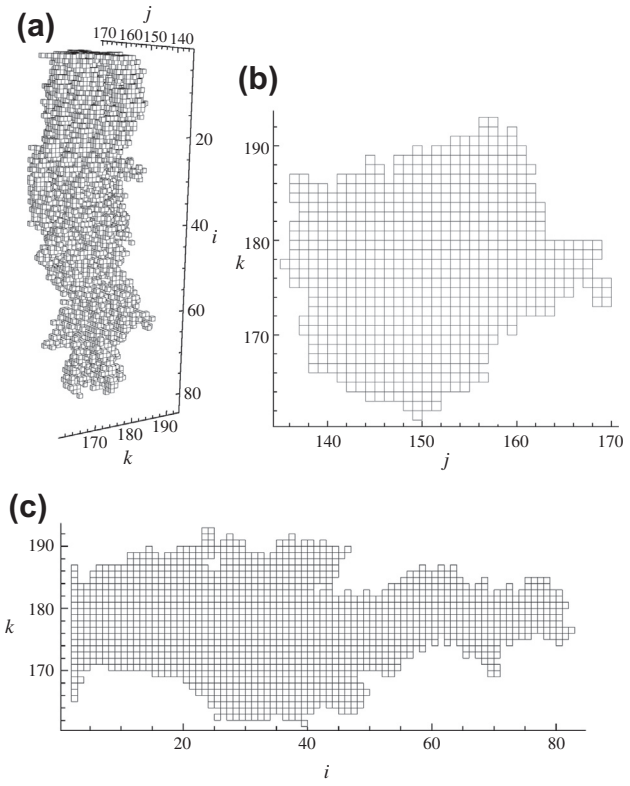

Fig. 10. Pit in metal surface after 200 s: (a) pit in 3D, (b) projection on the j k-plane (top view) and (c) projection on the i k-plane (vertical cross-section).

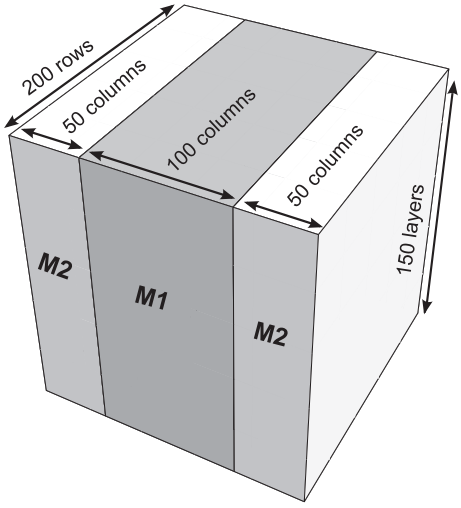

Fig. 11. Schematic representation of the bimetallic part of the 3D grid.

Table 3
Optimized model parameter values for the experimental data with different chloride concentrations.

	Mass percentage chloride ions		
Parameter	2.25%	2.5%	3.5%
ι	0.703	0.975	0.918
Δt	0.399	0.399	0.399
P_p	0.000278	0.000422	0.000201
P_{d0}	0.150	0.843	0.650
ζ	0.586	0.647	0.918

model, the remainder of this section will deal with an exemplary case study for the pitting corrosion of a bimetal.

Table 4
Bimetallic parameters for the weaker metal (M1) and the stronger metal (M2).

Parameter	M1	M2
P_p	0.4	0.2
P_{d0}	0.8	0.65
ζ	0.4	0.5

It is assumed here that the metal block of $\mathcal{G}$, i.e. layers two up to 151 in Fig. 5, is composed out of two types of metal. The first layer of $\mathcal{G}$ remains the aqueous layer. Fig. 11 shows layers two till 151 of $\mathcal{G}$ that will be used in the remainder of this section. The central part of the metal block (M1), i.e. columns 51 till 150, is chosen to be a weaker metal, meaning that it is more susceptible to corrosion, than the remaining columns of the metal block (M2). This difference in resistance to corrosion is expressed in the choice of parameter values. Since ι and Δt do not depend on the type of metal, they are chosen to be 0.918 and 0.399, respectively, while for the three remaining parameters a different value is chosen for each type of metal (see Table 4).

Simulations are performed with the stochastic CA-based model with a mass percentage of chloride ions of 3.5% and with a maximum number of pits equal to 25. Fig. 12(a)–(c) show the simulated

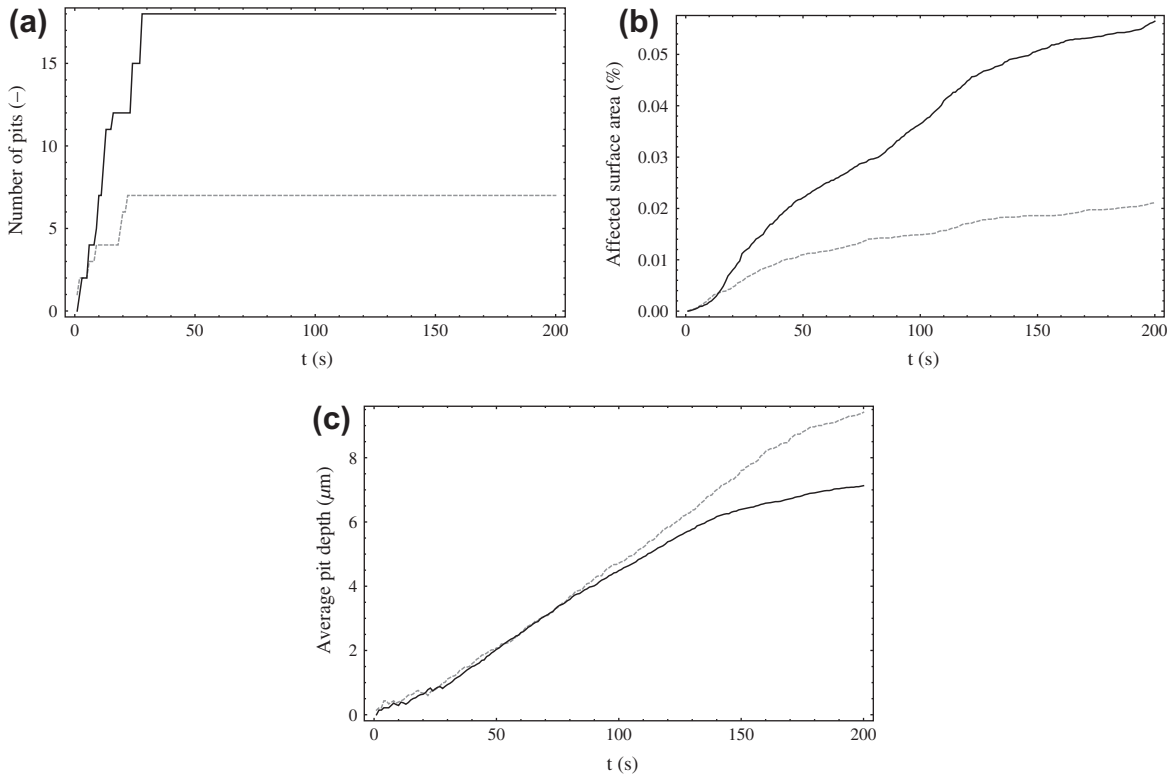

Fig. 12. Simulated outcome with the CA-based model for a bimetal with: (a) number of pits originating in M1 (black) and M2 (gray, dashed), (b) affected surface of M1 (black) and M2 (gray, dashed) and (c) average pits depth of pit originating in M1 (black) and M2 (gray, dashed).

time series of data for both types of metal. It can be seen that more pits are initiated on M1 than on M2 and moreover, that the surface of M1 is more affected than that of M2 in function of time. However, it is seen from Fig. 12 (c) that the average pit depth is larger for pits initiated in M2 than for those that are initiated in M1. This is explained by the fact that with the chosen parameter values, pits in M2 are deeper and more narrow, while pits in M1 are wider and more shallow. Of all the metal cells that are corroded (either by pit initiation or pit propagation), 58% belonged to M1.

Further, when studying the pits that grow in the different types of metal, it can be seen that pits that start in M1 continue on in M1 (see Fig. 13(a)). Pits that initially start in M2 on the other hand, often find a way into M1 and have a branch of the pit in this part as well (see Fig. 13(b)).

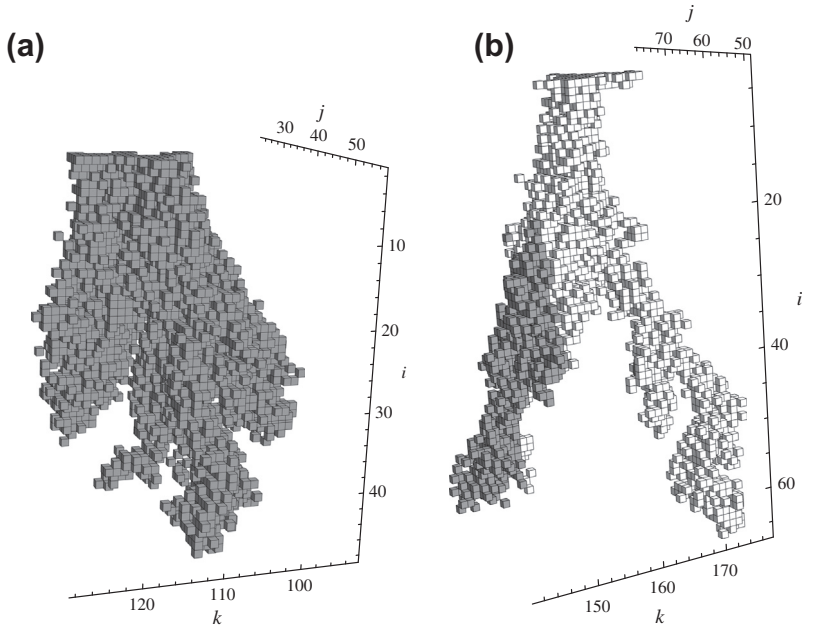

Fig. 13. Bimetalic 3D pit growth of a pit initiated in (a) M1 (gray) and (b) M2 (white).

4. Conclusion

The developed CA-based model with the incorporation of the key processes of pitting corrosion enables the simulation of pit growth in 3D. A sensitivity analysis showed that all parameters incorporated into the model are non-redundant and, moreover, the information obtained from this analysis was used to facilitate the parameter estimation. Via a grid search in two steps, the inverse problem of finding a set of parameters that gives rise to three simulated time series as close as possible to the three experimental time series, obtained by the authors in the laboratory, was solved. Further, the influence of the chloride concentration on the calibrated model parameters was investigated. Finally, the potential of the CA-based model was illustrated by means of a case study where pitting corrosion of a bimetalic material was studied.

However, it is clear that the fitting of the simulated results to the experimental ones is subject to further improvement. Depending on the degree of accuracy desired of the model, new parts can be added to the transition function of the CA, most likely coupled with the addition of more model parameters, which would possibly improve accuracy, but make the parameter estimation more difficult. It is therefore crucial to get more insights into the pitting corrosion phenomenon and the CA-based model before adding new parts to the transition function. Model simulations can be used to generate and/or test hypotheses as such increasing the knowledge on the phenomenon. Nevertheless, experimental data is important to test the validity and necessity of additions and/or changes to the model.

The most limiting point of the model at this point is the initiation of pits, both in the number of pits as their position and shape. In the current version of the model, the total number of pits is limited by the user, based on the experimental data. Nevertheless, it would be an improvement to the model if the process that stops new pits from appearing, is incorporated into the transition function. If more data were available, this process could possibly be learned from those data. Secondly, the shape of the pit at the surface is more or less circular (see Fig. 10(b)), although this is not necessarily so in reality. Finally, the positions at which new pits appear are at present randomly distributed over the surface (with the exception of the cathodically protected zone around the existing pits). Therefore, the integration of information on the experimental metal surface would ameliorate the model since new pits are preferentially formed along scratches and other impurities on the metal electrode.

Finally, it is stressed that the experimental data employed in this paper stem from a low number of replicated experiments such that little information on the uncertainty of these data is available. Data on more processes and more replications could help to discover new elements to be added to the model as well as to improve the modeling of the processes already incorporated into the model.

Acknowledgments

Pieter Van der Weeën is a doctoral researcher of the Ghent University Research Fund (BOF). The Brazilian authors gratefully acknowledge financial support from the FAPESP (process 2011/19430-0), CNPq and CAPES.

References

[1] J.R. Davis, Corrosion: Understanding the Basics, ASM International, 2000.
[2] G. Contreras, S. Goidanich, S. Maggi, C. Piccardi, M.V. Diamanti, M.P. Pedeferri, L. Lazzari, Representing localized corrosion processes through cellular automata, Corros. Rev. 29 (2011) 241–245.
[3] R. Landolfo, L. Cascini, F. Portiolo, Modeling of metal structure corrosion damage: a state of the art report, Sustainability 2 (2010) 2163–2175.
[4] P. Marcus, V. Maurice, H. Strehblow, Localized corrosion (pitting): a model of passivity breakdown including the role of the oxide layer nanostructure, Corros. Sci. 50 (2008) 2698–2704.
[5] T.P. Hoar, The production and breakdown of the passivity of metals, Corros. Sci. 7 (1967) 341–355.
[6] S.M. Sharland, A review of the theoretical modeling of crevice and pitting corrosion, Corrosion 27 (1987) 289–323.
[7] G.S. Frankel, Pitting corrosion of metals: a review of the critical factors, J. Electrochem. Soc. 145 (1998) 2186–2198.
[8] Z. Szklarska-Smialowska, Pitting corrosion of metals, NACE, Houston, Texas, 1986.
[9] G. Riedel, C. Voigt, H. Werner, K. Erkel, M. Günzel, The influence of acid soluble sulfide inclusions on the passivation behavior of austenitic Cr–Ni stainless steel, Corros. Sci. 27 (1987) 533–544.
[10] Z.Y. Liu, X.G. Li, Y.F. Cheng, In situ characterization of the electrochemistry of grain and grain boundary of an X70 steel in a near-neutral pH solution, Electrochem. Commun. 12 (2010) 936–938.
[11] L.L. Shreir, R.A. Jarman, G.T. Burstein, Corrosion: Corrosion Control, Butterworth Heinemann, 1994.
[12] I.A. Chaves, R.E. Melchers, Pitting corrosion in pipeline steel weld zones, Corros. Sci. 53 (2011) 4026–4032.
[13] M. Reuter, K.E. Heusler, Statistical investigations of the pitting of passive iron, Electrochim. Acta 35 (1990) 1809–1814.
[14] V. Vignal, H. Krawiec, O. Heintz, R. Oltra, The use of local electrochemical probes and surface analysis methods to study the electrochemical behavior and pitting corrosion of stainless steels, Electrochim. Acta 52 (2007) 4994–5001.
[15] S.M. Ghahari, A.J. Davenport, T. Rayment, T. Suter, J. Tinnes, C. Padovani, J.A. Hammons, M. Stampanoni, F. Marone, R. Mokso, In situ synchrotron X-ray micro-tomography study of pitting corrosion in stainless steel, Corros. Sci. 53 (2011) 2684–2687.
[16] L.J. Korb, Metals Handbook, Ninth ed., Asm Intl, 1987.
[17] B. Malki, B. Baroux, Computer simulation of the corrosion pit growth, Corros. Sci. 47 (2005) 171–182.
[18] H.W. Pickering, The significance of the local electrode potential within pits, crevices and cracks, Corros. Sci. 29 (1989) 325–341.
[19] H. Wang, B. Song, L. Wang, G. Lv, Three dimensional cellular automaton for simulation of the multi-pit corrosion damage evolution, Adv. Sci. Lett. 4 (2011) 2980–2985.
[20] A. Jarrah, M. Bigerelle, G. Guillemot, D. Najjar, A. Iost, J. Nianga, A generic statistical methodology to predict the maximum pit depth of a localized corrosion process, Corros. Sci. 53 (2011) 2453–2467.
[21] C. Punckt, M. Bölscher, H.H. Rotermund, A.S. Mikhailov, L. Organ, N. Budiansky, J.R. Scully, J.L. Hudson, Sudden onset of pitting corrosion on stainless steel as a critical phenomenon, Science 305 (2004) 1133–1136.
[22] A.M. Zimer, M.A. Carra, E.C. Rios, E.C. Pereira, L.H. Mascaro, Initial stages of corrosion pits on AISI 1040 steel in sulfide solution analyzed by temporal series micrographs coupled with electrochemical techniques, Corros. Sci. 76 (2013) 27–34.
[23] Y. González-García, G.T. Burstein, S. González, R.M. Souto, Imaging metastable pits on austenitic stainless steel in situ at the open-circuit corrosion potential, Electrochem. Commun. 6 (2004) 637–642.
[24] World Corrosion Organization – WCO. <http://www.corrosion.org/>.
[25] P.R. Roberge, Corrosion Engineering: Principles and Practice, McGraw-Hill Professional, 2008.
[26] A. Turnbull, D.A. Horner, B.J. Connolly, Challenges in modeling the evolution of stress corrosion cracks from pits, Eng. Fract. Mech. 76 (2009) 633–640.
[27] D.E. Williams, C. Westcott, M. Fleischmann, Studies of the initiation of pitting corrosion on stainless steels, J. Electroanal. Chem. 180 (1984) 549–564.
[28] T. Okada, A theory of pertubation-initiated pitting, J. Electrochem. Soc. 125 (1978) 1382–1388.
[29] B.G. Ateya, H.W. Pickering, Effects of ionic migration on the concentrations and mass-transfer rate in the diffusion layer of dissolving metals, J. Appl. Electrochem. 11 (1981) 453–461.
[30] T.R. Beck, E.A. Grens, An electrochemical mass transport-kinetic model for stress corrosion cracking of titanium, J. Electrochem. Soc. 116 (1969) 177–184.
[31] S.M. Sharland, C.P. Jackson, A.J. Driver, A finite-element model of the propagation of corrosion crevices and pits, Corros. Sci. 29 (1989) 1149–1166.
[32] P. Smith, S. Roy, S. Swailes, S. Maxwell, D. Page, J. Lawson, A model for the corrosion of steel subjected to synthetic produced water containing sulfate, chloride and hydrogen sulfide, Chem. Eng. Sci. 66 (2011) 5775–5790.
[33] J. Cai, R.A. Cottis, S.B. Lyon, Phenomenological modeling of atmosperic corrosion using an artificial neural network, Corros. Sci. 41 (1999) 2001–2030.
[34] W. Zhang, S. Ruan, D.A. Wolfe, G.S. Frankel, Statistical model for intergranular corrosion growth kinetics, Corros. Sci. 45 (2003) 353–370.
[35] J. Stafiej, D. di Caprio, L. Bartosik, Corrosion–passivation processes in a cellular automata based simulation study, J. Supercomput. 65 (2013) 697–709.
[36] I.G. Main, J.R. Henderson, P.G. Meredith, P.R. Sammonds, Self-organized criticality and fluid–rock interactions in the brittle field, Pure Appl. Geophys. 142 (1994) 529–543.
[37] S. Gobron, N. Chiba, 3D surface cellular automata and their applications, J. Vis. Comput. Animat. 10 (1999) 143–158.

[38] L. Bartosik, D. di Caprio, J. Stafiej, Cellular automata approach to corrosion and passivity phenomena, Pure Appl. Chem. 85 (2013) 247–256.
[39] J. Saunier, A. Chaussé, J. Stafiej, J.P. Badiali, Simulations of diffusion limited corrosion at the metal-environment interface, J. Electroanal. Chem. 563 (2004) 239–247.
[40] R.M. Pidaparti, M.J. Palakal, L. Fang, Cellular automata approach to aircraft corrosion growth, Int. J. Artif. Intell. Tools 14 (2005) 361–369.
[41] K.C. Lan, Y.T. Chen, T.C. Hung, H.M. Tung, G.P. Yu, Simulation of the growth of oxide layer of stainless steels with chromium using cellular automaton model: verification and parameter study, Comp. Mater. Sci. 77 (2013) 139–144.
[42] S.V. Lishchuk, R. Akid, K. Worden, J. Michalski, A cellular automaton model for predicting intergranular corrosion, Corros. Sci. 53 (2011) 2518–2526.
[43] L. Berec, Techniques of spatially explicit individual-based models: construction, simulation and mean-field analysis, Ecol. Modell. 150 (2002) 55–81.
[44] S. Wolfram, Statistical mechanics of cellular automata, Rev. Mod. Phys. 55 (1983) 601–644.
[45] Z. Vasilkoski, C.D. Weaver, A generator of protein folding kinetics states for the diffusion-collision model, J. Comput. Chem. 21 (2000) 923–932.
[46] L. Preziosi, Modeling and Simulation, Chapman & Hall, Boca Raton, United States, 2003.
[47] P. Van der Weeën, J.M. Baetens, J. Verwaeren, X. Van Doorslaer, P.M. Heynderickx, J. Dewulf, B. De Baets, Modeling the photocatalytic degradation of moxifloxacin by means of a stochastic cellular automaton, Chem. Eng. J. 188 (2012) 181–190.
[48] J. Milne, S.C. Fu, Epidemic modeling using cellular automata, in: Proceedings of the 1st Australian Conference on Artificial Life, 2003, pp. 43–57.
[49] C. Picioreanu, M. van Loosdrecht, J. Heijnen, Mathematical modeling of biofilm structure with a hybrid differential-discrete cellular automaton approach, Biotechnol. Bioeng. 58 (1998) 101–116.
[50] J. Schiff, Cellular Automata: A Discrete View of the World, John Wiley & Sons Ltd., Chichester, United Kingdom, 2008.
[51] S. El Yacoubi, A. El Jai, Cellular automata and spreadability, Math. Comput. Modell. 36 (2002) 1059–1074.
[52] T. Toffoli, Cellular automata as an alternative to (rather than an approximation of) differential equations in modeling physics, Physica D 10 (1984) 117–127.
[53] A. Salcido (Ed.), Cellular Automata – Innovative Modeling for Science and Engineering, InTech, 2011.
[54] P. Córdoba-Torres, R.P. Nogueira, L. de Miranda, L. Brenig, J. Wallenborn, V. Fairn, Cellular automaton simulation of a simple corrosion mechanism: mesoscopic heterogeneity versus macroscopic homogeneity, Electrochim. Acta 46 (2001) 2975–2989.
[55] C.G. Chase, Fluvial landsculpting and the fractal dimension of topography, Geomorphology 5 (1992) 39–57.
[56] C. Vautrin-Ul, H. Mendy, A. Taleb, A. Chaussé, J. Stafiej, J.P. Badiali, Numerical simulations of spatial heterogeneity formation in metal corrosion, Corros. Sci. 50 (2008) 2149–2158.
[57] J.M. Baetens, P. Van der Weeën, B. De Baets, Effects of asynchronous updating in cellular automata, chaos, Solit. Fract. 45 (2012) 383–394.
[58] A.M. Zimer, E.C. Rios, P.D. Mendes, W.N. Gonçalves, O.M. Bruno, E.C. Pereira, L.H. Mascaro, Investigation of AISI 1040 steel corrosion in H_2S solution containing chloride ions by digital image processing coupled with electrochemical techniques, Corros. Sci. 53 (2011) 3193–3201.
[59] A.M. Zimer, E.C. Rios, L.H. Mascaro, E.C. Pereira, Temporal series micrographs coupled with polarization curves to study pit corrosion, Electrochem. Commun. 13 (2011) 1484–1487.
[60] A.M. Zimer, M.A. Carra, L.H. Mascaro, E.C. Pereira, Temporal series of micrographs coupled with electrochemical techniques to analyze pitting corrosion of AISI 1040 steel in carbonate and chloride solutions, Electrochem. Acta. (accepted).
[61] A. Mokhtari, H.C. Frey, Sensitivity analysis of a two-dimensional probabilistic risk assessment model using analysis of variance, Risk Anal. 25 (2005) 1511–1529.
[62] A. Saltelli, M. Ratto, S. Tarantola, F. Campolongo, Sensitivity analysis for chemical models, Chem. Rev. 105 (2005) 2811–2827.
[63] A.B. Massada, Y. Carmel, Incorporating output variance in local sensitivity analysis for stochastic models, Ecol. Modell. 213 (2008) 463–467.
[64] M.D. Morris, Factorial sampling plans for preliminary computational experiments, Technometrics 33 (1991) 161–174.
[65] H. Liu, F. Yang, C. Huang, H. Fang, Y. Cheng, Sensitivity analysis of the semi-empirical model for the growth of the indigenous *Acidithiobacillus thiooxidans*, Chem. Eng. J. 129 (2007) 105–112.
[66] M.V. Ruano, J. Ribes, J. Ferrer, G. Sin, Application of the Morris method for screening the influential parameters of fuzzy controllers applied to wastewater treatment plants, Water Sci. Technol. 63 (2011) 2199–2206.
[67] F. Campolongo, J. Cariboni, A. Saltelli, An effective screening design for sensitivity analysis of large models, Environ. Modell. Softw. 22 (2007) 1509–1518.
[68] I. Merelli, D. Pescini, E. Mosca, P. Cazzaniga, C. Maj, G. Mauri, L. Milanesi, Grid computing for sensitivity analysis of stochastic biological models, Lect. Notes Comput. Sc. 6873 (2011) 62–73.
[69] J. Bergstra, Y. Bengio, Random search for hyper-parameter optimization, J. Mach. Learn. Res. 13 (2012) 281–305.
[70] P. Van der Weeën, N. De Clercq, J.M. Baetens, C. Delbaere, K. Dewettinck, B. De Baets, A discrete stochastic model for oil migration in chocolate-coated confectionery, J. Food Eng. 117 (2013) 602–610.
[71] I.M. Sobol, Distribution of points in a cube and approximate evaluation of integrals, USSR Comput. Maths. Math. Phys. 7 (1967) 86–112.
[72] K. Beven, J. Freer, Equifinality, data assimilation, and uncertainty estimation in mechanistic modeling of complex environmental systems using the GLUE methodology, J. Hydrol. 249 (2001) 11–29.